

PIE: Simulating Disease Progression via Progressive Image Editing

Kaizhao Liang^{*†}, Xu Cao^{*‡}, Kuei-Da Liao, Tianren Gao, Zhengyu Chen, Tejas Nama

[†] University of Texas, Austin

[‡] University of Illinois, Urbana Champaign

kaizhaol@utexas.edu

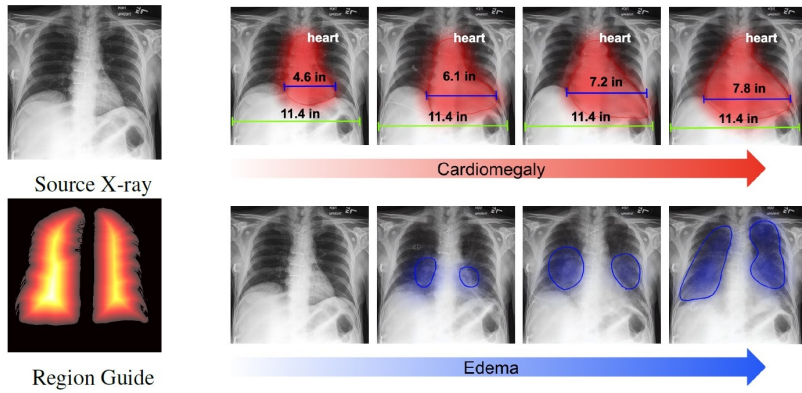


Figure 1: Illustrative examples of disease progression simulation using PIE. The top progression sequence depicts a patient's heart increasing in size (red), indicating Cardiomegaly. The bottom sequence demonstrates the expanding mass areas (blue) in a patient's lung, indicating Edema.

Abstract

The trajectories of disease progression could greatly affect the quality and efficacy of clinical diagnosis, prognosis, and treatment. However, one major challenge is the lack of longitudinal medical imaging monitoring of individual patients over time. To address this issue, we develop a novel framework termed Progressive Image Editing (PIE) that enables controlled manipulation of disease-related image features, facilitating precise and realistic disease progression simulation in imaging space. Specifically, we leverage recent advancements in text-to-image generative models to simulate disease progression accurately and personalize it for each patient. We theoretically analyze the iterative refining process in our framework as a gradient descent with an exponentially decayed learning rate. To validate our framework, we conduct experiments in three medical imaging domains. Our results demonstrate the superiority of PIE over existing methods such as Stable Diffusion Video and Style-Based Manifold Extrapolation based on CLIP score (Realism) and Disease Classification Confidence (Alignment). Our user study collected feedback from 35 veteran physicians to assess the generated progressions. Remarkably, 76.2% of the feedback agrees with the fidelity of the generated progressions. To our best knowledge, PIE is the first method to generate disease progression images without sequential training data. PIE can allow healthcare providers to model disease imaging trajectories over time, predict future treatment responses, and improve patient outcomes.

1 Introduction

Understanding disease progression is of utmost importance in the field of healthcare and medical research. Disease progression refers to the way a particular illness evolves and changes over time within an individual's body. By studying the progression of diseases, healthcare professionals can develop effective treatment strategies and interventions. It enables them to predict the course of the disease, identify potential complications, and adjust treatment plans accordingly. Additionally, understanding disease progression helps in the development of new drugs and therapies, as researchers can target specific stages or mechanisms of the disease. Furthermore, monitoring disease progression allows healthcare providers to assess the efficacy of treatments, measure the impact of interventions, and make informed decisions about patient care. Ultimately, a comprehensive understanding of disease progression is essential for improving patient outcomes, advancing medical knowledge, and finding innovative approaches to prevent and treat diseases.

However, simulating disease progression poses a formidable challenge in the realm of medical research, primarily due to the lack of continuous monitoring of individual patients over time and high cost to collect longitudinal data [Sukkar et al., 2012, Wang et al., 2014, Liu et al., 2015, Cook and Bies, 2016, Severson et al., 2020]. The intricate and multifaceted dynamics of disease progression, combined with the lack of comprehensive and continuous monitoring of individual patients, result in the absence of established methodologies. Disease progression encompasses intricate spatial changes, morphological transformations, and functional alterations over time, all of which are influenced by an array of factors including genetics, environment, and behavior [Hinrichs et al., 2011, Ray, 2011, Lee et al., 2019]. The integration of multiple data sources and modalities, such as imaging and clinical reports, is imperative to holistically depict the intricate and evolving nature of disease progression. Moreover, disease progression exhibits significant variability and heterogeneity across patients and disease subtypes, rendering a uniform approach impractical. Despite the considerable challenges, simulating disease progression carries substantial implications for clinical diagnosis, prognostication, and therapeutic intervention [Barrett et al., 2022]. Accurate simulation facilitates a deeper understanding of the underlying mechanisms driving disease pathogenesis, enables the identification of optimal treatment strategies, and facilitates the prediction of patient outcomes. As such, this area of research assumes pivotal importance in advancing medical science and elevating patient care standards. Consequently, our primary focus lies in the development of a novel framework for accurate and individualized simulation of disease progression by effectively integrating text and image modalities without continuous monitoring of individual patients over time.

Past disease progression research is grounded on variations of the Hidden Markov Model (HMM) [Liu et al., 2015] and deep probabilistic models [Alaa and van der Schaar, 2019]. While the disease trajectories in these models are interpretable thanks to their focus on transitional probabilities between disease states, they fail to simulate visually comprehensible symptoms. Moreover, these studies have limitations in terms of their ability to incorporate textual information and generate individualized predictions based on individualized conditions, and they can not handle imaging data. This highlights the need for more advanced and flexible simulation frameworks to accurately capture the complex and dynamic nature of disease progression visually. To incorporate textural information into a conditioned simulation of disease progression, we propose a progressive framework PIE, for disease progression simulation that combines text and image modalities. Specifically, we aim to progressively add and subtract disease-related features, controlled by text, to conditionally progress the disease without significantly altering the original base image features (see Figure 1). Since our framework is built based on the invertibility of DDIM [Song et al., 2020a], our theoretical analysis shows it can be seen as a gradient descent toward the objective maximum log-likelihood of given text conditioning. The learning rate in this iterative process is decaying exponentially with each iteration forward, which means that the algorithm is effectively exploring the solution space while maintaining a balance between convergence speed and stability. This theoretical analysis guarantees that our framework is moving the instance toward the targeted manifold and ensures modification is bounded.

Moreover, we empirically evaluate PIE on three distinct medical imaging datasets, including CheXpert [Irvin et al., 2019], Diabetic Retinopathy Detection [CHF, 2015] and ISIC 2018 [Codella et al., 2019]. We demonstrate that our framework leads to more accurate and individualized predictions of disease progression on these datasets, which can potentially improve clinical diagnosis, treatment planning, and patient outcomes. We also conduct a user study with veteran physicians to evaluate the effectiveness of our proposed framework for disease progression simulation. The study aimed to

assess the accuracy and quality of the simulated disease progressions generated by our framework and to determine how well they matched real-world standards. The study involves presenting the physicians with a set of simulated disease images and progressions and then asking them to assess the accuracy and quality of each generated image and progression. The highlight from the study shows 76.2% of the physicians agree with the simulated disease progressions generated by our framework, indicating they are closely matching physicians' expectations.

Overall, our framework has the potential to be a valuable tool for medical research and clinical practice, having the potential to contribute to the development of more effective treatments and better patient outcomes. Our main contributions are listed as follows:

- We propose a novel framework PIE, which allows for more precise and controllable manipulation of disease-related image features and leads to more accurate and individualized disease progression simulation.
- We provide theoretical evidence that our iterative refinement process is equivalent to gradient descent with an exponentially decaying learning rate, which helps to establish a deeper understanding of the underlying mechanism of our method and provides a basis for further optimization and improvement of the approach.
- We demonstrate the superior performance of PIE over baselines in disease progression prediction with three medical domains. The results show that PIE produces more accurate and high-quality disease progression prediction.
- We also conduct a user study with veteran physicians to evaluate the effectiveness of our proposed framework for disease progression simulation. Remarkably, 76.2% of the physicians agree with the simulated disease progressions generated by our framework, indicating they are closely matching real-world expectations.

2 Background

Denoising Diffusion Probabilistic Models (DDPM) [Ho et al., 2020] are a class of generative models that use a diffusion process to transform a simple initial distribution, such as a Gaussian, into the target data distribution. The model assumes that the data points are generated by iteratively applying a diffusion process to a set of latent variables x_1, \dots, x_T in a sample space χ . At each time step t , Gaussian noise is added to the latent variables x_t , and the variables are then transformed back to the original space using a learned invertible transformation function. This process is repeated for a fixed number of steps to generate a final output. The latent variable models can be expressed in the following form,

$$p_\theta(x_0) = \int p_\theta(x_{0:T}) dx_{1:T}, \quad \text{where } p_\theta(x_{0:T}) \prod_{t=1}^T p_\theta^{(t)}(x_{t-1}|x_t) \quad (1)$$

Because of a special property of the forward process,

$$q(x_t|x_0) = \int q(x_{1:t}|x_0) dx_{1:(t-1)} = \mathcal{N}(x_t; \sqrt{\alpha_t}x_0, (1 - \alpha_t) \cdot \mathbf{I}) \quad (2)$$

we can express x_t as a linear combination of x_0 and a noise variable ϵ , which is the key to enabling the image editing process.

$$x_t = \sqrt{\alpha_t} \cdot x_0 + \sqrt{1 - \alpha_t} \cdot \epsilon, \quad \text{where } \epsilon \sim \mathcal{N}(\mathbf{0}, \mathbf{I}) \quad (3)$$

Denoising Diffusion Implicit Models (DDIM) [Song et al., 2020a] that uses a non-Markovian forward process to generate data. Unlike Denoising Diffusion Probabilistic Models (DDPM), DDIM does not require explicit modeling of the latent variables. Instead, the model generates samples by solving a non-linear differential equation, which defines a continuous-time evolution of the data distribution. We can express its forward process as follows,

$$q_\sigma(x_{1:T}|x_0) := q_\sigma(x_T|x_0) \prod_{t=2}^T q_\sigma(x_{t-1}|x_t, x_0) \quad (4)$$

where $q_\sigma(x_{t-1}|x_t, x_0) = \mathcal{N}(\sqrt{\alpha_t}x_0, (1 - \alpha_t)\mathbf{I})$ and for all $t > 1$

$$q_\sigma(x_{t-1}|x_t, x_0) = \mathcal{N}(\sqrt{\alpha_{t-1}x_0} + \sqrt{1 - \alpha_{t-1} - \sigma_t^2} \cdot \frac{x_t - \sqrt{\alpha_t}x_0}{\sqrt{1 - \alpha_t}}, \sigma_t^2\mathbf{I}) \quad (5)$$

Setting $\sigma_t = 0$, it defines a generation process going from x_t to x_{t-1} as follows

$$x_{t-1} = \sqrt{\alpha_{t-1}} \left(\frac{x_t - \sqrt{1 - \alpha_t} \epsilon_\theta^{(t)}(x_t)}{\sqrt{\alpha_t}} \right) + \sqrt{1 - \alpha_{t-1}} \cdot \epsilon_\theta^{(t)}(x_t) \quad (6)$$

where the $\epsilon_\theta^{(t)}(x_t)$ is a model that attempts to predict $\epsilon_t \sim \mathcal{N}(\mathbf{0}, \mathbf{I})$ from x_t

Guided Image Editing via Diffusion [Meng et al., 2021, Lugmayr et al., 2022, Couairon et al., 2022] are general techniques that aim to modify either the entirety or certain parts of images through diffusion. The process commences by introducing noise to the genuine base image and subsequently applying the reverse diffusion process to remove the noise, resulting in the production of photo-realistic images. Specifically, we employ the DDIM forward process 3 for the addition of noise and the reverse process 6 for one cycle of image modification, as demonstrated in 1.

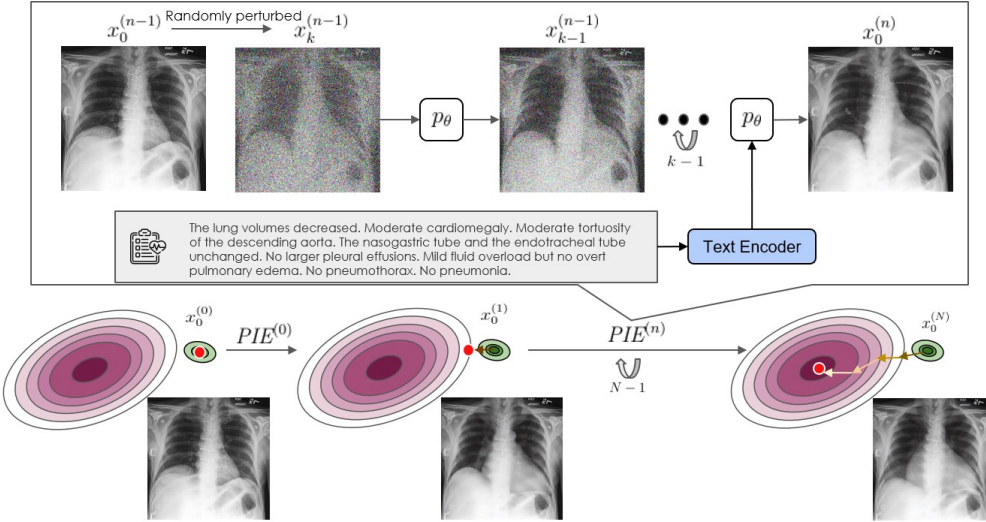


Figure 2: Overview of the PIE pipeline. PIE is illustrated using an example of disease progression editing X-ray from a healthy state to cardiomegaly. For any given step n in PIE, we first utilize DDIM inversion to procure an inverted noise map. Subsequently, we denoise it using clinical reports imbued with progressive cardiomegaly information. The output of DDIM denoising serves as the input for step $n + 1$, thus ensuring a gradual and controllable disease progression simulation. After simulating N steps, the image is converged to the final state.

3 Progressive Image Editing

Progressive image editing (PIE) is a novel framework proposed to refine and enhance images in an iterative and discrete manner, allowing the use of additional prompts for small and precise adjustments to simulate semantic modification while keeping realism. Unlike traditional image editing techniques, PIE involves a multi-stage process where each step builds upon the previous one, with the aim of achieving a final result that is more refined and smooth than if all changes were made at once. The approach also enables precise control over specific semantic features of the image to be adjusted without significant impacts on other regions. The main purpose of PIE is to simulate disease progression from multi-modal input data.

Procedure. The inputs to PIE are a medical image $x_0^{(0)}$ depicting any start or middle stage of a disease and a corresponded clinical report y as the text conditioning [Rombach et al., 2022], which could either be real or simulated, providing the potential trajectory of the patient’s disease progression.

The output generated is a sequence of images, $\{x_0^{(0)}, x_0^{(1)}, \dots, x_0^{(N)}\}$, illustrating the progression of the disease as per the input report. The iterative PIE procedure is defined as follows:

Proposition 1 Let $x_0^{(N)} \sim \chi$, where χ is distribution of photo-realistic images, y be the text conditioning, running $PIE^{(n)}(\cdot, \cdot)$ recursively is denoted as following, where $N \geq n \geq 1$,

$$x_0^{(n)} = PIE^{(n)}(x_0^{(n-1)}, y) \quad (7)$$

Then, the resulting output $x_0^{(N)}$ maximizes the posterior probability $p(x_0^{(N)} | y)$.

With each round of editing as shown in Figure 2, the image gets closer to the objective by moving in the direction of $-\nabla \log p(x|y)$. Due to the properties of DDIM, the step size would gradually decrease with a constant factor. Additional and more detailed proofs will be available in Supplementary A.

Detailed algorithm. We present the single-step PIE in Algorithm 1. For $PIE^{(n)}$, we define α_k according to the DDIM case. Line 8 in Algorithm 1 ensures progressive and limited modifications between the original input image $x_0^{(0)}$, the single-step edited output x' , and the region guide selector M_{ROI} through the utilization of interpolation average parameters β_1 and β_2 . These parameters dictate the modification ratio between the ROI mask-guided space and the original input space. As β_1 increases, the multi-step editing process becomes smoother, though it may sacrifice some degree of realism.

Medical heuristic guidance. PIE can be particularly useful for disease progressions, where medical images such as X-rays or Retinopathy need to be edited to track the progression of a disease over time. During the simulation, the region guide masks play a big role as prior information. Unlike other randomly inpainting tasks [Lugmayr et al., 2022], ROI mask for medical imaging can be extracted from real or synthetic clinical reports Boag et al. [2020], Lovelace and Mortazavi [2020] using domain-specific Segment Anything models [Kirillov et al., 2023, Ma and Wang, 2023]. It helps keep unrelated regions consistent through the progressive changes using PIE or baseline models. In order to generate sequential disease imaging data, PIE uses noise strength γ to control the influence from the patient’s clinically reported and expected treatment regimen at time n . N is used to control the duration of the disease occurrence or treatment regimen. PIE allows the user to make such controls over the iterative process, and running $PIE^{(n)}$ multiple times can improve the accuracy of disease imaging tracking and reduce the likelihood of missed or misinterpreted changes. Related ablation study for M_{ROI} , γ , N , β_1 , β_2 will be available in Supplementary D.

Baselines To our knowledge, there are no existing image editing models specifically designed for simulating disease progression. To underscore the unique strengths of PIE, we compare it against two of the most promising state-of-the-art methods Stable Diffusion Walk (SD Walk) [Raw, 2022] and Style-Based Manifold Extrapolation (Extrapolation) [Han et al., 2022] for generating progressive images as our baselines. During the comparison, all baseline methods are using the same Stable Diffusion weights and also applied M_{ROI} for region guided. More details about the baseline models are available in Supplementary B.

Algorithm 1: Progressive Image Editing n -th step ($PIE^{(n)}$)

Input: Original input image $x_0^{(0)}$ at the start point, input image $x_0^{(n-1)}$ at stage n , number of diffusion steps T , text conditional vector y , noise strength γ , stable diffusion parameterized denoiser ϵ_θ , a ROI mask M_{ROI} , $M_{ROI}^{i,j} \in [0, 1]$

Output: Modified image x' as x_0^n

- 1 $x' \leftarrow x_0^{(n-1)}$
- 2 $k \leftarrow \gamma \cdot T$
- 3 $\epsilon \sim \mathcal{N}(0, \mathcal{I})$
- 4 $x' \leftarrow \sqrt{\alpha_k} \cdot x' + \sqrt{1 - \alpha_k} \cdot \epsilon$
- 5 **for** $t = k$ **to** 1 **do**
- 6 $x' \leftarrow \sqrt{\alpha_{t-1}} \left(\frac{x' - \sqrt{1 - \alpha_t} \epsilon_\theta^{(t)}(x', y)}{\sqrt{\alpha_t}} \right) + \sqrt{1 - \alpha_{t-1}} \cdot \epsilon_\theta^{(t)}(x', y)$
- 7 **end**
- 8 $x' \leftarrow (\beta_1 \cdot (x' - x_0^{(0)}) + x_0^{(0)}) \cdot (1 - M_{ROI}) + (\beta_2 \cdot (x' - x_0^{(0)}) + x_0^{(0)}) \cdot M_{ROI}$
- 9 **return** x' **as** $x_0^{(n)}$

4 Experiment

In this section, we present experiments on various disease progression tasks. Experiments results demonstrate that PIE can simulate the disease-changing trajectory that is influenced by different medical conditions. Notably, PIE also preserves unrelated visual features from the original medical imaging report, even as it progressively edits the disease representation. Figure 3 showcases a set of disease progression simulation examples across three distinct types of medical imaging. Details for Stable Diffusion fine-tuning, pretraining model for confidence metrics settings will be available in Supplementary C.

Table 1: Comparisons with multi-step editing simulations. The backbone of PIE and baseline approaches are Stable Diffusion with the same pre-trained weight.

Method	Chest X-ray		Retinopathy		Skin Lesion Image	
	Conf (\uparrow)	CLIP-I (\uparrow)	Conf (\uparrow)	CLIP-I (\uparrow)	Conf (\uparrow)	CLIP-I (\uparrow)
PIE	0.690	0.96	0.807	0.99	0.453	0.95
SD Walk	0.389	0.92	0.121	0.89	0.201	0.88
Extrapolation	0.0543	0.97	0.0742	0.99	0.226	0.95

4.1 Experimental Setups

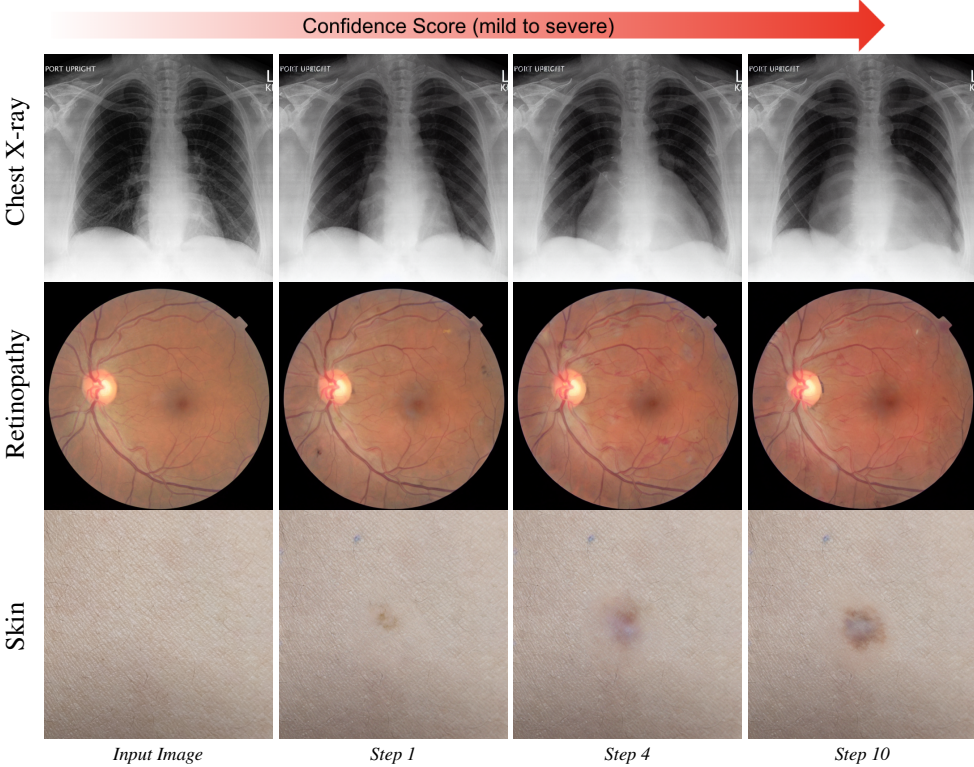


Figure 3: Disease Progression Simulation of PIE. The top progression is for Cardiomegaly. The middle progression is for Diabetic Retinopathy. The bottom progression is for Melanocytic Nevus.

Datasets for Disease Progression. We validate the disease progression analysis through end-to-end medical domain-specific image inference. Specifically, we evaluate the pretrained domain-specific stable diffusion model on three different types of disease datasets in classification tasks: CheXpert for chest X-ray classification [Irvin et al., 2019], ISIC 2018 / HAM10000 [Codella et al., 2019, Tschandl et al., 2018] for skin cancer prediction, and Kaggle Diabetic Retinopathy Detection Challenge [CHF, 2015]. Each of these datasets presents unique challenges and differ in scale, making them suitable for

testing the robustness and versatility of PIE. We also collected over 30 healthy data among the test set from these datasets. These data were used for disease progression simulation. Three groups of progression visualization results can be found in Figure 3.

Evaluation Metrics. The assessment of generated disease progression images relies on two crucial aspects: alignment to edited disease feature and subject fidelity. To measure these characteristics, we utilize two primary metrics: the CLIP-I score and the classification confidence score. The CLIP-I score represents the average pairwise cosine similarity between the CLIP embeddings of generated and real images [Radford et al., 2021, Ruiz et al., 2022]. The classification confidence score is determined using supervised train deep networks for binary classification between negative (healthy) and positive (disease) samples. It is denoted as $\text{Conf} = \text{Sigmoid}(f_\theta(x))$ and represent whether the simulation results are aligned to target disease. In our experiments, we train the DeepAUC maximization method [Yuan et al., 2021] (state-of-the-art of Chexpert and ISIC 2018 task 3) using DenseNet121 [Huang et al., 2017] as the backbone to compute the classification confidence score.

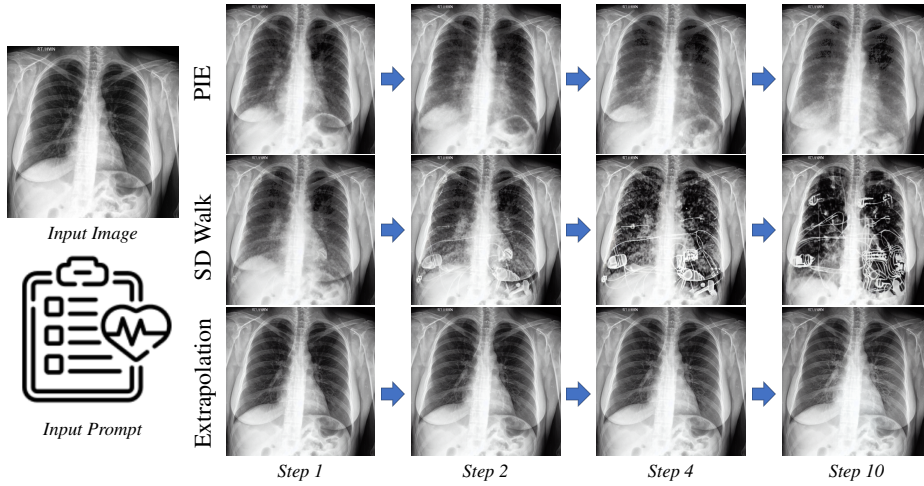


Figure 4: Using PIE, SD Walk, Extrapolation to simulate Edema progression with clinical reports as input prompt.

4.2 Progression Simulation Comparison

In order to demonstrate the superior performance of PIE in disease progression simulation over other single-step editing methods, we perform experiments on six different diseases using the datasets previously mentioned. For each disease, we used 10 healthy samples in the test set as simulation start point and run PIE, SD Walk, Extrapolation with 5 random seeds. We obtain at least 50 disease imaging trajectories for each patient. Table 1 showcases that PIE consistently surpasses both SD Walk and Extrapolation in terms of disease confidence scores while maintaining high CLIP-I scores. For Chexpert dataset, the 0.690 final confidence score is the average score among 5 classes. For Diabetic Retinopathy and HAM10000 datasets, we compare PIE with SD Walk, Extrapolation for editing image to the most common seen class since these datasets are highly imbalanced. Figure 5 illustrates the evolution of disease confidence scores during the progression simulation in each step. We observe that PIE is able to produce more faithful and realistic progressive editing compared to the other two baselines. Interestingly, while the CLIP-I score of Extrapolation is comparable to that of PIE, it fails to effectively edit the key disease features of the input images as its confidence scores are low throughout and at the end of the progression.

Figure 4 showcases a group of progression simulation results for Edema in chest X-rays with the input prompt, "Edema lung finding is shown in the chest cavity." It is evident from our observations that

Table 2: In order to quantitatively analyze the responses of experienced physicians, we consider each pathology class as independent and calculate the precision, recall, and F1 score across all pathologies and physicians.

Data	Precision	Recall	F1
Real	0.505	0.415	0.455
PIE	0.468	0.662	0.549

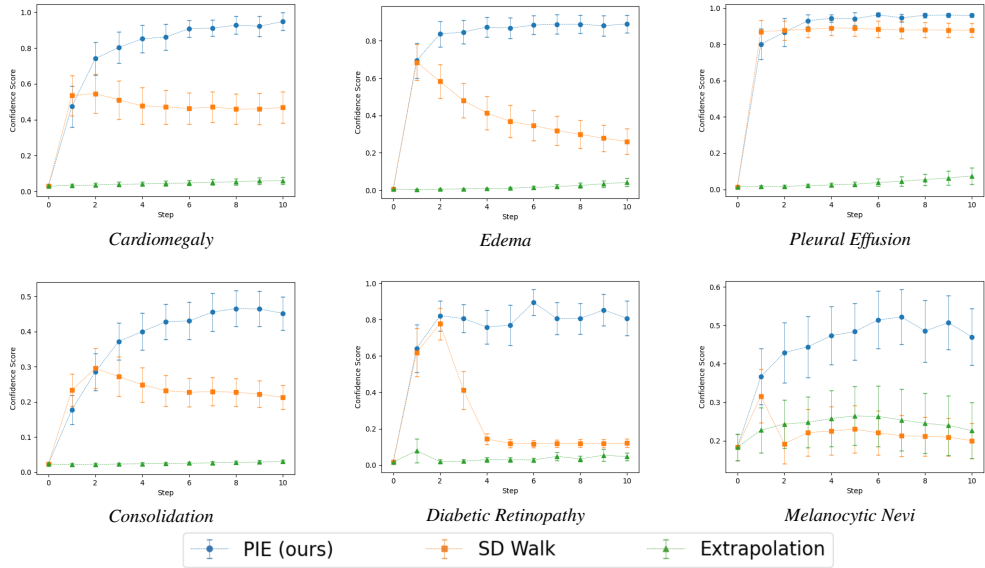


Figure 5: PIE excels in comparison to all the baseline methods across six different disease progression simulations. The inputs utilized are genuine healthy images from the test sets. For each image, we apply five random seeds to simulate disease progression over ten steps. The confidence score, a value that ranges from 0 to 1, signifies the classification confidence for a specific disease.

while SD Walk can significantly alter the input image in the initial step, it fails to identify the proper direction of progression in the manifold after a few steps and would easily create uncontrollable noise. Conversely, Extrapolation only brightens the Chest X-ray without making substantial modifications. PIE, on the other hand, not only convincingly simulates the disease trajectory but also manages to preserve unrelated visual features from the original medical imaging. Further visual comparisons and analysis are presented in Supplementary D.

4.3 User Study

To further assess the quality of our generated images, we ask 35 veteran physicians with 14.4 years of experience on average to answer a questionnaire on chest X-rays. The questionnaire includes disease classifications on the generated and real X-ray images as well as evaluations of the realism of generated disease progression sequences of Cardiomegaly, Edema, and Pleural Effusion. More details of the questionnaire are presented in Supplementary E.1. The participating physicians have agreed with a probability of **76.2%** that the simulated progressions on the targeted diseases fit their expectations.

Table 2 provides an interesting insight into experienced physicians' performance in predicting the pathology on real and generated X-rays. Details of the calculations of the statistics could be found in Supplementary E.2. Surprisingly, we find users' performance on generated X-rays is superior to their performance on real images, with substantially higher recall and F1. In addition, the statistical test suggests that the F1 scores of generated scans are significantly higher (p-value of 0.0038) than the real scans. One plausible explanation is due to the nature of PIE, the result of running progressive image editing makes pathological features more evident. The superiority of PIE is consistent with the 76% probability that the participating physicians agree the generated sequences correspond to the disease progressions as shown in Figure 6. The aggregated results from

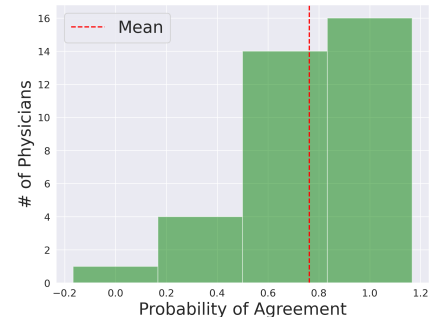


Figure 6: Distribution of probability of agreement to the generated progressions among 35 veteran physicians.

the user study demonstrate our framework’s ability to simulate disease progression to meet real-world standards.

5 Related Works

Disease Progression Simulation Longitudinal disease progression data derived from individual electronic health records offer an exciting avenue to investigate the nuanced differences in the progression of diseases over time [Schulam and Arora, 2016, Stankeviciute et al., 2021, Chen et al., 2022, Mikhael et al., 2023]. Most of the previous works are based on HMM [Wang et al., 2014, Liu et al., 2015, Alaa et al., 2017] and deep probabilistic models [Alaa and van der Schaar, 2019]. Some recent works start to resolve disease progression simulation by using diffusion probabilistic models. [Raj et al., 2015] utilized a diffusion model to predict the progression of Alzheimer’s disease based on changes in brain metabolism over time, demonstrating high accuracy in predicting future disease status. [Wu et al., 2017] used a similar approach to predict the progression of Huntington’s disease based on patterns of brain atrophy observed in MRI scans. However, all these methods struggle to handle complex modalities such as imaging data and fail to address personalized healthcare. Moreover, disease progression modeling methods often require plenty of time-series data in treatment effect estimation to train, and the lack of such time-series data, in reality, poses a significant challenge for disease progression simulation [Xue et al., 2020, Chen, 2022, Berrevoets et al., 2023].

Generative Adversarial Networks Generative models like Variational Autoencoders (VAEs) [Kingma and Welling, 2013] and Generative Adversarial Networks (GANs) [Goodfellow et al., 2020] have been widely employed in medical imaging applications [Nie et al., 2017, Isola et al., 2017, Cao et al., 2020]. GAN-based image editing models, where they edit the image by manipulating latent vectors, typically focus on a single-step editing task, such as style transfer [Fetty et al., 2020] based on StyleGAN [Karras et al., 2019, 2020]. Recent GAN models [Kang et al., 2023, Patashnik et al., 2021] have harnessed the power of CLIP [Radford et al., 2021] embedding to guide image editing based on contextual prompts. However, GAN-based models are unstable and difficult to optimize in general.

Denoising Diffusion Models [Sohl-Dickstein et al., 2015, Ho et al., 2020, Song et al., 2020a, Rombach et al., 2022, Karras et al., 2022] have become increasingly popular in recent years due to their ability to create photo-realistic images from textual descriptions. These models can be used for a wide range of applications, from generating artwork [Rombach et al., 2022, Saharia et al., 2022] to creating simulations of the physical world [Luo and Hu, 2021, Poole et al., 2022, Tevet et al., 2022]. One major advantage of these models is their ability to learn from large-scale datasets. Among the various text-to-image models, Stable Diffusion [Rombach et al., 2022] has received considerable attention because of its impressive performance in generating high-quality images and its relatively low cost to fine-tune. Its denoising process works similarly to the diffusion models but in a latent space, and this process results in a final image that is highly consistent with the input text, making it an excellent tool for text-guided image editing. Diffusion models can also be effortlessly incorporated into an image-to-image editing pipeline [Brooks et al., 2022, Parmar et al., 2023, Orgad et al., 2023], thus providing users the ability to edit scenarios across multiple modalities and assess potential imaging progressive editing paths. However, existing image-to-image methods can only be used for single-step editing, which is difficult to simulate time-series progression data.

6 Conclusion

In conclusion, our proposed framework, Progressive Image Editing (PIE), holds great potentials as a tool for medical research and clinical practice in simulating disease progression. By leveraging recent advancements in text-to-image generative models and fine-tuned Stable Diffusion, PIE achieves high fidelity and personalized disease progression simulations. The theoretical analysis shows that the iterative refining process is equivalent to gradient descent with an exponentially decayed learning rate, and practical experiments on three medical imaging datasets demonstrate that PIE surpasses baseline methods, such as SD Walk and Extrapolation, in several quantitative metrics. Furthermore, a user study conducted with veteran physicians confirms that the simulated disease progressions generated by PIE meet real-world standards. To the best of our knowledge, our approach is the first of its kind to offer clinically meaningful disease progression simulations using medical imaging data in an iterative image editing context. Despite current limitations due to the lack of continuous

monitoring data and detailed medical reports, our framework has vast potential in modeling disease trajectories over time, restoring missing data from previous treatments, predicting future treatment responses, and ultimately improving patient outcomes. Moving forward, we aim to incorporate more data with richer descriptions and different monitoring modalities, such as chemical biomarkers and physiological recordings, into fine-tuning Stable Diffusion, enabling our framework to more precise control over disease simulation through text conditioning.

References

Diabetic Retinopathy Detection, howpublished= <https://www.kaggle.com/c/diabetic-retinopathy-detection>, 2015.

Ahmed M Alaa and Mihaela van der Schaar. Attentive state-space modeling of disease progression. *Advances in neural information processing systems*, 32, 2019.

Ahmed M Alaa, Scott Hu, and Mihaela Schaar. Learning from clinical judgments: Semi-markov-modulated marked hawkes processes for risk prognosis. In *International Conference on Machine Learning*, pages 60–69. PMLR, 2017.

Jeffrey S Barrett, Tim Nicholas, Karim Azer, and Brian W Corrigan. Role of disease progression models in drug development. *Pharmaceutical Research*, 39(8):1803–1815, 2022.

Jeroen Berrevoets, Fergus Imrie, Trent Kyono, James Jordon, and Mihaela van der Schaar. To impute or not to impute? missing data in treatment effect estimation. In *International Conference on Artificial Intelligence and Statistics*, pages 3568–3590. PMLR, 2023.

William Boag, Tzu-Ming Harry Hsu, Matthew McDermott, Gabriela Berner, Emily Alesentzer, and Peter Szolovits. Baselines for chest x-ray report generation. In *Machine learning for health workshop*, pages 126–140. PMLR, 2020.

Tim Brooks, Aleksander Holynski, and Alexei A Efros. Instructpix2pix: Learning to follow image editing instructions. *arXiv preprint arXiv:2211.09800*, 2022.

Bing Cao, Han Zhang, Nannan Wang, Xinbo Gao, and Dinggang Shen. Auto-gan: self-supervised collaborative learning for medical image synthesis. In *Proceedings of the AAAI conference on artificial intelligence*, volume 34, pages 10486–10493, 2020.

Irene Y Chen. *Machine Learning Approaches for Equitable Healthcare*. PhD thesis, Massachusetts Institute of Technology, 2022.

Irene Y Chen, Rahul G Krishnan, and David Sontag. Clustering interval-censored time-series for disease phenotyping. In *Proceedings of the AAAI Conference on Artificial Intelligence*, volume 36, pages 6211–6221, 2022.

Noel Codella, Veronica Rotemberg, Philipp Tschandl, M Emre Celebi, Stephen Dusza, David Gutman, Brian Helba, Aadi Kalloo, Konstantinos Liopyris, Michael Marchetti, et al. Skin lesion analysis toward melanoma detection 2018: A challenge hosted by the international skin imaging collaboration (isic). *arXiv preprint arXiv:1902.03368*, 2019.

Sarah F Cook and Robert R Bies. Disease progression modeling: key concepts and recent developments. *Current pharmacology reports*, 2:221–230, 2016.

Guillaume Couairon, Jakob Verbeek, Holger Schwenk, and Matthieu Cord. Diffedit: Diffusion-based semantic image editing with mask guidance. *arXiv preprint arXiv:2210.11427*, 2022.

Lukas Fetty, Mikael Bylund, Peter Kuess, Gerd Heilemann, Tufve Nyholm, Dietmar Georg, and Tommy Löfstedt. Latent space manipulation for high-resolution medical image synthesis via the stylegan. *Zeitschrift für Medizinische Physik*, 30(4):305–314, 2020.

Ian Goodfellow, Jean Pouget-Abadie, Mehdi Mirza, Bing Xu, David Warde-Farley, Sherjil Ozair, Aaron Courville, and Yoshua Bengio. Generative adversarial networks. *Communications of the ACM*, 63(11):139–144, 2020.

Tianyu Han, Jakob Nikolas Kather, Federico Pedersoli, Markus Zimmermann, Sebastian Keil, Maximilian Schulze-Hagen, Marc Terwoelbeck, Peter Isfort, Christoph Haarburger, Fabian Kiessling, et al. Image prediction of disease progression for osteoarthritis by style-based manifold extrapolation. *Nature Machine Intelligence*, pages 1–11, 2022.

Chris Hinrichs, Vikas Singh, Guofan Xu, Sterling C Johnson, Alzheimers Disease Neuroimaging Initiative, et al. Predictive markers for ad in a multi-modality framework: an analysis of mci progression in the adni population. *Neuroimage*, 55(2):574–589, 2011.

Jonathan Ho, Ajay Jain, and Pieter Abbeel. Denoising diffusion probabilistic models. *Advances in Neural Information Processing Systems*, 33:6840–6851, 2020.

Gao Huang, Zhuang Liu, Laurens Van Der Maaten, and Kilian Q Weinberger. Densely connected convolutional networks. In *Proceedings of the IEEE conference on computer vision and pattern recognition*, pages 4700–4708, 2017.

Jeremy Irvin, Pranav Rajpurkar, Michael Ko, Yifan Yu, Silviana Ciurea-Ilcus, Chris Chute, Henrik Marklund, Behzad Haghgoo, Robyn Ball, Katie Shpanskaya, et al. Chexpert: A large chest radiograph dataset with uncertainty labels and expert comparison. In *Proceedings of the AAAI conference on artificial intelligence*, volume 33, pages 590–597, 2019.

Phillip Isola, Jun-Yan Zhu, Tinghui Zhou, and Alexei A Efros. Image-to-image translation with conditional adversarial networks. In *Proceedings of the IEEE conference on computer vision and pattern recognition*, pages 1125–1134, 2017.

Minguk Kang, Jun-Yan Zhu, Richard Zhang, Jaesik Park, Eli Shechtman, Sylvain Paris, and Taesung Park. Scaling up gans for text-to-image synthesis. *arXiv preprint arXiv:2303.05511*, 2023.

Tero Karras, Samuli Laine, and Timo Aila. A style-based generator architecture for generative adversarial networks. In *Proceedings of the IEEE/CVF conference on computer vision and pattern recognition*, pages 4401–4410, 2019.

Tero Karras, Samuli Laine, Miika Aittala, Janne Hellsten, Jaakko Lehtinen, and Timo Aila. Analyzing and improving the image quality of stylegan. In *Proceedings of the IEEE/CVF conference on computer vision and pattern recognition*, pages 8110–8119, 2020.

Tero Karras, Miika Aittala, Timo Aila, and Samuli Laine. Elucidating the design space of diffusion-based generative models. *arXiv preprint arXiv:2206.00364*, 2022.

Diederik P Kingma and Max Welling. Auto-encoding variational bayes. *arXiv preprint arXiv:1312.6114*, 2013.

Alexander Kirillov, Eric Mintun, Nikhila Ravi, Hanzi Mao, Chloe Rolland, Laura Gustafson, Tete Xiao, Spencer Whitehead, Alexander C Berg, Wan-Yen Lo, et al. Segment anything. *arXiv preprint arXiv:2304.02643*, 2023.

Garam Lee, Kwangsik Nho, Byungkon Kang, Kyung-Ah Sohn, and Dokyoon Kim. Predicting alzheimer’s disease progression using multi-modal deep learning approach. *Scientific reports*, 9(1):1952, 2019.

Yu-Ying Liu, Shuang Li, Fuxin Li, Le Song, and James M Rehg. Efficient learning of continuous-time hidden markov models for disease progression. *Advances in neural information processing systems*, 28, 2015.

Ilya Loshchilov and Frank Hutter. Sgdr: Stochastic gradient descent with warm restarts. *arXiv preprint arXiv:1608.03983*, 2016.

Ilya Loshchilov and Frank Hutter. Decoupled weight decay regularization. *arXiv preprint arXiv:1711.05101*, 2017.

Justin Lovelace and Bobak Mortazavi. Learning to generate clinically coherent chest x-ray reports. In *Findings of the Association for Computational Linguistics: EMNLP 2020*, pages 1235–1243, 2020.

Andreas Lugmayr, Martin Danelljan, Andres Romero, Fisher Yu, Radu Timofte, and Luc Van Gool. Repaint: Inpainting using denoising diffusion probabilistic models. In *Proceedings of the IEEE/CVF Conference on Computer Vision and Pattern Recognition*, pages 11461–11471, 2022.

Shitong Luo and Wei Hu. Diffusion probabilistic models for 3d point cloud generation. In *Proceedings of the IEEE/CVF Conference on Computer Vision and Pattern Recognition*, pages 2837–2845, 2021.

Jun Ma and Bo Wang. Segment anything in medical images. *arXiv preprint arXiv:2304.12306*, 2023.

Chenlin Meng, Yutong He, Yang Song, Jiaming Song, Jiajun Wu, Jun-Yan Zhu, and Stefano Ermon. Sdedit: Guided image synthesis and editing with stochastic differential equations. In *International Conference on Learning Representations*, 2021.

Peter G Mikhael, Jeremy Wohlwend, Adam Yala, Ludvig Karstens, Justin Xiang, Angelo K Takigami, Patrick P Bourguoin, PuiYee Chan, Sofiane Mrah, Wael Amayri, et al. Sybil: a validated deep learning model to predict future lung cancer risk from a single low-dose chest computed tomography. *Journal of Clinical Oncology*, pages JCO–22, 2023.

Dong Nie, Roger Trullo, Jun Lian, Caroline Petitjean, Su Ruan, Qian Wang, and Dinggang Shen. Medical image synthesis with context-aware generative adversarial networks. In *Medical Image Computing and Computer Assisted Intervention- MICCAI 2017: 20th International Conference, Quebec City, QC, Canada, September 11-13, 2017, Proceedings, Part III 20*, pages 417–425. Springer, 2017.

Hadas Orgad, Bahjat Kawar, and Yonatan Belinkov. Editing implicit assumptions in text-to-image diffusion models. *arXiv preprint arXiv:2303.08084*, 2023.

Gaurav Parmar, Krishna Kumar Singh, Richard Zhang, Yijun Li, Jingwan Lu, and Jun-Yan Zhu. Zero-shot image-to-image translation. *arXiv preprint arXiv:2302.03027*, 2023.

Or Patashnik, Zongze Wu, Eli Shechtman, Daniel Cohen-Or, and Dani Lischinski. Styleclip: Text-driven manipulation of stylegan imagery. In *Proceedings of the IEEE/CVF International Conference on Computer Vision (ICCV)*, pages 2085–2094, October 2021.

Ben Poole, Ajay Jain, Jonathan T Barron, and Ben Mildenhall. Dreamfusion: Text-to-3d using 2d diffusion. *arXiv preprint arXiv:2209.14988*, 2022.

Alec Radford, Jong Wook Kim, Chris Hallacy, Aditya Ramesh, Gabriel Goh, Sandhini Agarwal, Girish Sastry, Amanda Askell, Pamela Mishkin, Jack Clark, et al. Learning transferable visual models from natural language supervision. In *International conference on machine learning*, pages 8748–8763. PMLR, 2021.

Ashish Raj, Eve LoCastro, Amy Kuceyeski, Duygu Tosun, Norman Relkin, Michael Weiner, Alzheimer’s Disease Neuroimaging Initiative (ADNI, et al. Network diffusion model of progression predicts longitudinal patterns of atrophy and metabolism in alzheimer’s disease. *Cell reports*, 10(3):359–369, 2015.

Nathan Raw. Stable diffusion videos. <https://github.com/nateraw/stable-diffusion-videos>, 2022.

Pritha Ray. Multimodality molecular imaging of disease progression in living subjects. *Journal of biosciences*, 36:499–504, 2011.

Robin Rombach, Andreas Blattmann, Dominik Lorenz, Patrick Esser, and Björn Ommer. High-resolution image synthesis with latent diffusion models. In *Proceedings of the IEEE/CVF Conference on Computer Vision and Pattern Recognition*, pages 10684–10695, 2022.

Nataniel Ruiz, Yuanzhen Li, Varun Jampani, Yael Pritch, Michael Rubinstein, and Kfir Aberman. Dreambooth: Fine tuning text-to-image diffusion models for subject-driven generation. *arXiv preprint arXiv:2208.12242*, 2022.

Chitwan Saharia, William Chan, Saurabh Saxena, Lala Li, Jay Whang, Emily L Denton, Kamyar Ghasemipour, Raphael Gontijo Lopes, Burcu Karagol Ayan, Tim Salimans, et al. Photorealistic text-to-image diffusion models with deep language understanding. *Advances in Neural Information Processing Systems*, 35:36479–36494, 2022.

Peter Schulam and Raman Arora. Disease trajectory maps. *Advances in neural information processing systems*, 29, 2016.

Kristen A Severson, Lana M Chahine, Luba Smolensky, Kenney Ng, Jianying Hu, and Soumya Ghosh. Personalized input-output hidden markov models for disease progression modeling. In *Machine Learning for Healthcare Conference*, pages 309–330. PMLR, 2020.

Jascha Sohl-Dickstein, Eric Weiss, Niru Maheswaranathan, and Surya Ganguli. Deep unsupervised learning using nonequilibrium thermodynamics. In *International Conference on Machine Learning*, pages 2256–2265. PMLR, 2015.

Jiaming Song, Chenlin Meng, and Stefano Ermon. Denoising diffusion implicit models. *arXiv preprint arXiv:2010.02502*, 2020a.

Yang Song, Jascha Sohl-Dickstein, Diederik P Kingma, Abhishek Kumar, Stefano Ermon, and Ben Poole. Score-based generative modeling through stochastic differential equations. *arXiv preprint arXiv:2011.13456*, 2020b.

Kamile Stankeviciute, Ahmed M Alaa, and Mihaela van der Schaar. Conformal time-series forecasting. *Advances in Neural Information Processing Systems*, 34:6216–6228, 2021.

Rafid Sukkar, Elyse Katz, Yanwei Zhang, David Raunig, and Bradley T Wyman. Disease progression modeling using hidden markov models. In *2012 annual international conference of the IEEE engineering in medicine and biology society*, pages 2845–2848. IEEE, 2012.

Guy Tevet, Sigal Raab, Brian Gordon, Yonatan Shafir, Daniel Cohen-Or, and Amit H Bermano. Human motion diffusion model. *arXiv preprint arXiv:2209.14916*, 2022.

Philipp Tschandl, Cliff Rosendahl, and Harald Kittler. The ham10000 dataset, a large collection of multi-source dermatoscopic images of common pigmented skin lesions. *Scientific data*, 5(1):1–9, 2018.

Xiang Wang, David Sontag, and Fei Wang. Unsupervised learning of disease progression models. In *Proceedings of the 20th ACM SIGKDD international conference on Knowledge discovery and data mining*, pages 85–94, 2014.

Dan Wu, Andreia V Faria, Laurent Younes, Susumu Mori, Timothy Brown, Hans Johnson, Jane S Paulsen, Christopher A Ross, Michael I Miller, PREDICT-HD Investigators, and Coordinators of the Huntington Study Group. Mapping the order and pattern of brain structural mri changes using change-point analysis in premanifest huntington’s disease. *Human brain mapping*, 38(10):5035–5050, 2017.

Yuan Xue, Nan Du, Anne Mottram, Martin Seneviratne, and Andrew M Dai. Learning to select best forecast tasks for clinical outcome prediction. *Advances in Neural Information Processing Systems*, 33:15031–15041, 2020.

Zhuoning Yuan, Yan Yan, Milan Sonka, and Tianbao Yang. Large-scale robust deep auc maximization: A new surrogate loss and empirical studies on medical image classification. In *Proceedings of the IEEE/CVF International Conference on Computer Vision*, pages 3040–3049, 2021.

A Theoretical Analysis

A.1 Proof of Proposition 1

In this proof, we follow the conventions and definitions in Song et al. [2020a]

$$x_{t-1} = \sqrt{\alpha_{t-1}} \left(\frac{x_t - \sqrt{1 - \alpha_t} \epsilon_\theta^{(t)}(x_t, y)}{\sqrt{\alpha_t}} \right) + \sqrt{1 - \alpha_{t-1}} \cdot \epsilon_\theta^{(t)}(x_t, y) \quad (8)$$

Now given a base image denoted as $x_0^{(0)}$, we wish to perform diffusion-based editing recursively for N times. The roll-back (to the k th-steps, where $k \geq 1$) according to (3):

$$x_k^{(n)} = \sqrt{\alpha_k} \cdot x_0^{(n-1)} + \sqrt{1 - \alpha_k} \cdot \epsilon \quad (9)$$

where $\epsilon \sim \mathcal{N}(0, \mathcal{I})$. Plugging (9) into (8),

$$\begin{aligned} x_{k-1}^{(n)} &= \sqrt{\alpha_{k-1}} \left(\frac{x_k^{(n)} - \sqrt{1 - \alpha_k} \epsilon_\theta^{(k)}(x_k^{(n)}, y)}{\sqrt{\alpha_k}} \right) + \sqrt{1 - \alpha_{k-1}} \cdot \epsilon_\theta^{(k)}(x_k^{(n)}, y) \\ &= \sqrt{\alpha_{k-1}} \cdot x_0^{(n-1)} + \sqrt{\frac{\alpha_{k-1}(1 - \alpha_k)}{\alpha_k}} \cdot (\epsilon - \epsilon_\theta^{(k)}(x_k^{(n)}, y)) + \sqrt{1 - \alpha_{k-1}} \cdot \epsilon_\theta^{(k)}(x_k^{(n)}, y) \end{aligned} \quad (10)$$

Setting $k = 1$ to perform the revert diffusion process

$$x_0^{(n)} = \sqrt{\alpha_0} \cdot x_0^{(n-1)} + \sqrt{\frac{\alpha_0(1 - \alpha_1)}{\alpha_1}} \cdot (\epsilon - \epsilon_\theta^{(1)}(x_1^{(n)}, y)) + \sqrt{1 - \alpha_0} \cdot \epsilon_\theta^{(1)}(x_1^{(n)}, y) \quad (11)$$

Unrolling this recursion in (11), we have

$$\begin{aligned} x_0^{(N)} &= (\sqrt{\alpha_0})^N \cdot x_0^{(0)} + \sqrt{\frac{\alpha_0(1 - \alpha_1)}{\alpha_1}} \cdot \sum_i^N (\sqrt{\alpha_0})^i \cdot \epsilon \\ &\quad + \frac{\sqrt{\alpha_1 - \alpha_0 \alpha_1} - \sqrt{\alpha_0 - \alpha_0 \alpha_1}}{\sqrt{\alpha_1}} \cdot \sum_i^N (\sqrt{\alpha_0})^i \cdot \epsilon_\theta^{(i)}(x_1^{(i)}, y) \end{aligned} \quad (12)$$

Typically, α_0 is set to a number close to but less than 1, where in the case of stable diffusion 0.9999, α_1 is 0.9995, assuming 50 step schedule.

The second term in (12) is a sampling from Gaussian distributions with geometrically decreasing variances.

$$\lim_{N \rightarrow \infty} \sum_i^N (\sqrt{\alpha_0})^i \cdot \epsilon = 0 \quad (13)$$

Given a large enough N ,

$$x_0^{(N)} \approx (\sqrt{\alpha_0})^N \cdot x_0^{(0)} + \frac{\sqrt{\alpha_1 - \alpha_0 \alpha_1} - \sqrt{\alpha_0 - \alpha_0 \alpha_1}}{\sqrt{\alpha_1}} \cdot \sum_i^N (\sqrt{\alpha_0})^i \cdot \epsilon_\theta^{(i)}(x_1^{(i)}, y) \quad (14)$$

Proposition 1 in Song et al. [2020a] declares "optimal $\epsilon_\theta^{(i)}$ has an equivalent probability flow ODE corresponding to the "Variance-Exploding" SDE in Song et al. [2020b]". Hence, $\epsilon_\theta^{(i)}(x_1^{(i)}, y) := \nabla_x \log p(x|y)$. This can be seen as gradient descent with a geometrically decaying learning rate with a factor of $\sqrt{\alpha_0}$, with "base learning rate" $\frac{\sqrt{\alpha_1 - \alpha_0 \alpha_1} - \sqrt{\alpha_0 - \alpha_0 \alpha_1}}{\sqrt{\alpha_1}}$.

Notice that in (14), there is a decaying factor on the initial image $x_0^{(0)}$, as N grows the original image will surely diminish. Therefore, some other empirical measures are required to preserve the structure of the image, such as segmentation masking, edit strength scheduling and etc.

A.2 Additional Theoretical Analysis

Proposition 2 Assuming $\|x_0^{(0)}\| \leq C_1$ and $\|\epsilon_\theta(x, y)\| \leq C_2$, $(x, y) \in (\chi, \Gamma)$, for any $\delta > 0$, if

$$n > \frac{2}{\log(\alpha_0)} \cdot (\log(\delta) - C) \quad (15)$$

then,

$$\|x_0^{(n+1)} - x_0^{(n)}\| < \delta \quad (16)$$

where, $\lambda = \frac{\sqrt{\alpha_0 - \alpha_0 \alpha_1} - \sqrt{\alpha_1 - \alpha_0 \alpha_1}}{\sqrt{\alpha_1}}$, χ is the image distribution, Γ is the text condition distribution, and $C = \log((\frac{1}{\sqrt{\alpha_0}} - 1) \cdot C_1 + \lambda \cdot C_2)$

Proof Continuing on 14, for any $n > 1$, we have

$$\begin{aligned} \|x_0^n - x_0^{n-1}\| &= \|(\sqrt{\alpha_0})^n \cdot [(1 - \frac{1}{\sqrt{\alpha_0}}) \cdot x_0^{(0)} - \lambda \cdot \epsilon_\theta^{(n)}(x_1^{(n)}, y)]\| \\ &\leq (\sqrt{\alpha_0})^n \cdot [\|(1 - \frac{1}{\sqrt{\alpha_0}}) \cdot x_0^{(0)}\| + \lambda \cdot \|\epsilon_\theta^{(n)}(x_1^{(n)}, y)\|] \\ &\leq (\sqrt{\alpha_0})^n [(\frac{1}{\sqrt{\alpha_0}} - 1) \cdot C_1 + \lambda \cdot C_2] \end{aligned} \quad (17)$$

to guarantee $\|x_0^n - x_0^{n-1}\| \leq \delta$, we just need to set,

$$\begin{aligned} (\sqrt{\alpha_0})^n [(\frac{1}{\sqrt{\alpha_0}} - 1) \cdot C_1 + \lambda \cdot C_2] &< \delta \\ \frac{n}{2} \log(\alpha_0) + \log((\frac{1}{\sqrt{\alpha_0}} - 1) \cdot C_1 + \lambda \cdot C_2) &< \log(\delta) \end{aligned} \quad (18)$$

hence, given that $\alpha_0 < 1$ and $\log(\alpha_0) < 0$

$$n > \frac{2}{\log(\alpha_0)} \cdot (\log(\delta) - \log((\frac{1}{\sqrt{\alpha_0}} - 1) \cdot C_1 + \lambda \cdot C_2)) \quad (19)$$

Let $C = \log((\frac{1}{\sqrt{\alpha_0}} - 1) \cdot C_1 + \lambda \cdot C_2)$, we have

$$n > \frac{2}{\log(\alpha_0)} \cdot (\log(\delta) - C) \quad (20)$$

From above, we can conclude that as n grows bigger the changes between steps would grow smaller. The difference between steps will get arbitrarily small.

Proposition 3 For all $N > 1$, $\|x_0^{(N)} - x_0^{(0)}\|$ is bounded by a constant κ . where $\kappa > 0$

Proof From 17 and applying triangle inequality, we observe that the difference is a sum of a geometric sequence scaled by a constant factor,

$$\begin{aligned} \|x_0^{(N)} - x_0^{(0)}\| &\leq \sum_{n=1}^N \|x_0^{(n)} - x_0^{(n-1)}\| \\ &\leq \sum_{n=1}^N (\sqrt{\alpha_0})^n [(\frac{1}{\sqrt{\alpha_0}} - 1) \cdot C_1 + \lambda \cdot C_2] \\ &= \frac{1 - (\sqrt{\alpha_0})^N}{1 - \sqrt{\alpha_0}} \cdot [(\frac{1}{\sqrt{\alpha_0}} - 1) \cdot C_1 + \lambda \cdot C_2] \end{aligned} \quad (21)$$

As N goes to infinity,

$$\lim_{N \rightarrow \infty} \|x_0^{(N)} - x_0^{(0)}\| \leq \frac{1}{1 - \sqrt{\alpha_0}} \cdot [(\frac{1}{\sqrt{\alpha_0}} - 1) \cdot C_1 + \lambda \cdot C_2] = \kappa \quad (22)$$

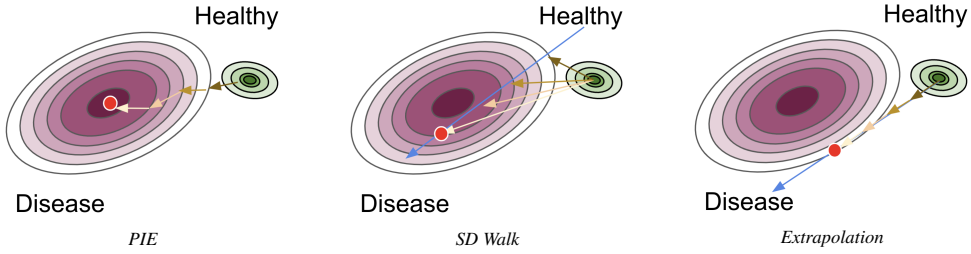


Figure 7: Editing path of PIE, SD Walk, and Extrapolation.

B Baselines

Stable Diffusion Walk (SD Walk) [Raw, 2022] and Style-Based Manifold Extrapolation (Extrapolation) are two leading techniques in the field of progressive video generation / medical image editing, each displaying promising results within specific domains. However, their applicability remains confined to these particular domains and poses a challenge in extending to the broader scope of different medical imaging data. To illustrate this, Figure 7 provides a comparative visualization of single-step editing using these three techniques.

Stable Diffusion Walk (SD Walk) [Raw, 2022] control the multi-step denoising process in the Stable Diffusion Videos pipeline. By smoothly and randomly traversing through the sampled latent space, SD Walk demonstrates its capability to generate a series of images that progressively align with a given text prompt (see Figure B). As the state-of-the-art publicly available pipeline, SD Walk can generate sequential imaging data by interpolating the latent space via multi-step Stable Diffusion. Though SD Walk is useful for general domain [Raw, 2022], it is not controllable for medical prompts.

Style-Based Manifold Extrapolation (Extrapolation) [Han et al., 2022], involves iteratively modifying images by extrapolating between two latent manifolds. To determine the directions of latent extrapolation, the nearest neighbors algorithm is employed on distributions of known trajectories. However, in cases where progression data is not readily available, as in the study at hand, the directions are obtained by randomly sampling and computing the mean of each manifold.

The actual interpolation of Extrapolation for each step can be defined as:

$$\Delta = \frac{1}{m} \sum_m^{i=1} \frac{\Delta t^i}{\Delta T} [G^{-1}(x_{(0)}^{(n+1)}) - G^{-1}(x_{(0)}^{(n)})] \quad (23)$$

where $G^{-1}(x_{(0)}^{(n)})$ is the corresponding latent vector of image at stage n.

C Experimental Settings

In the following sections, we detail the experimental setup used for training the Stable Diffusion model with domain-specific medical data. We also outline the design of our disease progression simulation experiment across three datasets, as well as provide an evaluation of the time costs.

C.1 Implementation Details

Both *PIE* and the baselines use publicly available Stable Diffusion checkpoints (CompVis/stable-diffusion-v1-4) that we further fine-tune on the training sets of each of the target datasets. Our code and checkpoints will be publicly available upon publication.

Stable Diffusion Training. To fine-tune the Stable Diffusion model, we center-crop and resize the input images to 512×512 resolution. We utilize the AdamW optimizer [Loshchilov and Hutter, 2017] with a weight decay set at 0.01. Additionally, we employ a cosine learning rate scheduler [Loshchilov and Hutter, 2016], with the base learning rate set at 5×10^{-5} . All models undergo fine-tuning for 20,000 steps on eight NVIDIA A100 GPUs, with each GPU handling a batch size of 8.

DeepAUC DenseNet121 Training. We have previously outlined the concept of a classification confidence score. In order to pre-train the DeepAUC DenseNet121 model, we utilize the original code repository provided by the authors. The model training process involves the use of an exponential learning rate scheduler, with the base learning rate set to 1×10^{-4} . Initially, the model is pre-trained on a multi-class task for each respective dataset. Subsequently, we employ the AUC loss proposed in the study by [Yuan et al., 2021] to finetune the binary classification task, distinguishing between negative (healthy) and positive (disease) samples. The AUC loss finetuning process involves the use of an exponential learning rate scheduler, with the base learning rate set to 1×10^{-2} . All models used for calculating classification confidence score are finetuned for 10 epochs on one NVIDIA A100 GPU, with a batch size of 128. For each class, the final classification accuracy on the validation set is 95.0 % using finetuned DenseNet121 model.

PIE progression simulation. The PIE progression simulation is tested with one NVIDIA A100 GPU. In the following sections, we will show the hyper-parameter search experiment for PIE and explain the insight to adjust them.

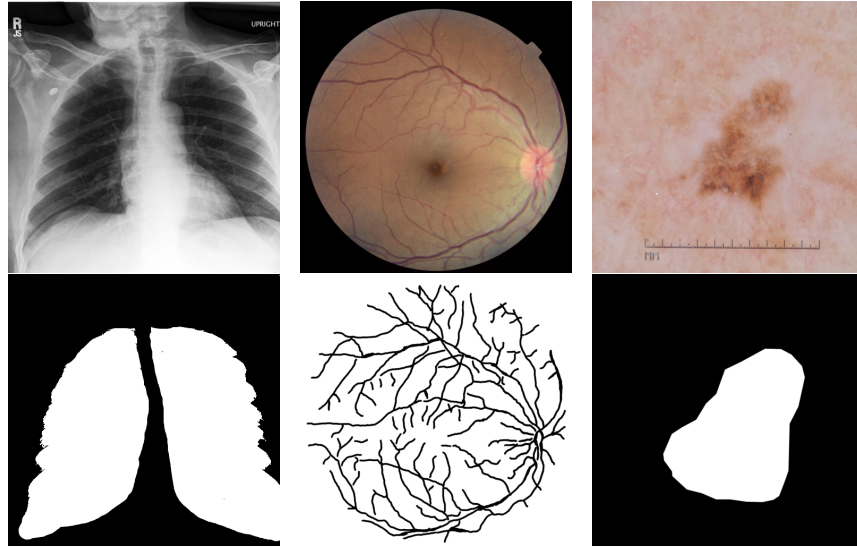


Figure 8: ROI masks for three different domains. Note, the white part in the mask is the disease-related regions.

C.2 ROI Mask Generation

The ROI Mask used in experiments are generated by Segment Anything Model (SAM) Kirillov et al. [2023] and modified to smooth the edge. For different domains, since the region guide prior is different, the mask shape and size is also different. Figure 8 showcases examples of ROI masks utilized for simulation in the PIE and baseline models.

C.3 Time Cost Analysis

Given that both PIE and the baseline methods utilize the same Stable Diffusion backbone Rombach et al. [2022], a comparison of latency among each method is unnecessary. For simulating disease progression on an image of size 512×512 , per step PIE requires approximately 0.078s to generate the subsequent stage when the strength parameter, γ , is set to 0.5, batch size is set to 1 and using one NVIDIA A100 (80GB).

D Ablation Study

To investigate the influence of each hyper-parameter in PIE and analyse the progression visualization, we conduct several ablation studies for visualization, failure cases analysis and hyperparameter searching.

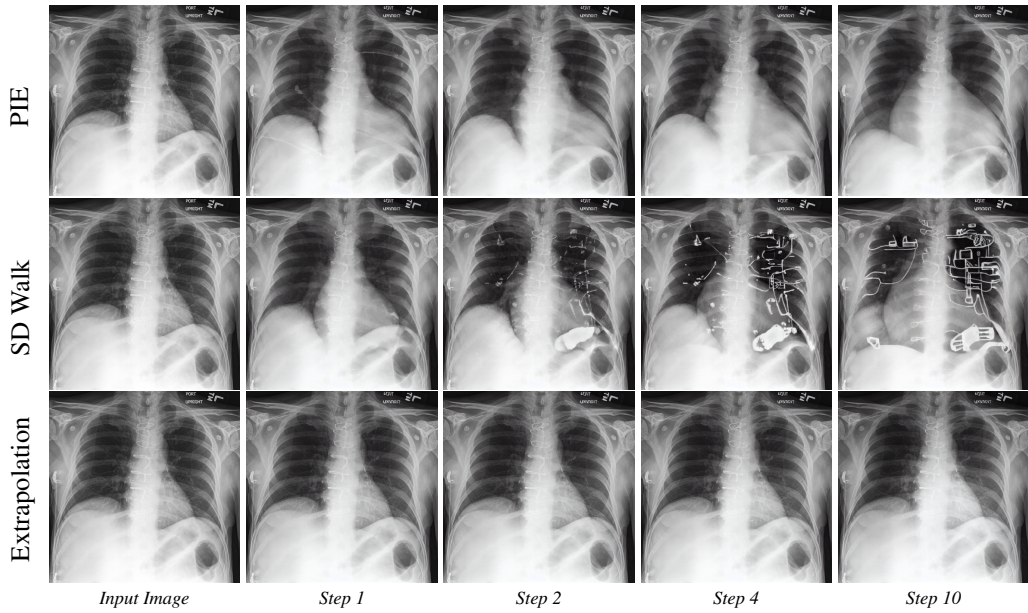


Figure 9: Visualization of PIE, SD Walk, Extrapolation to generate disease progression from Cardiomegaly clinical reports.

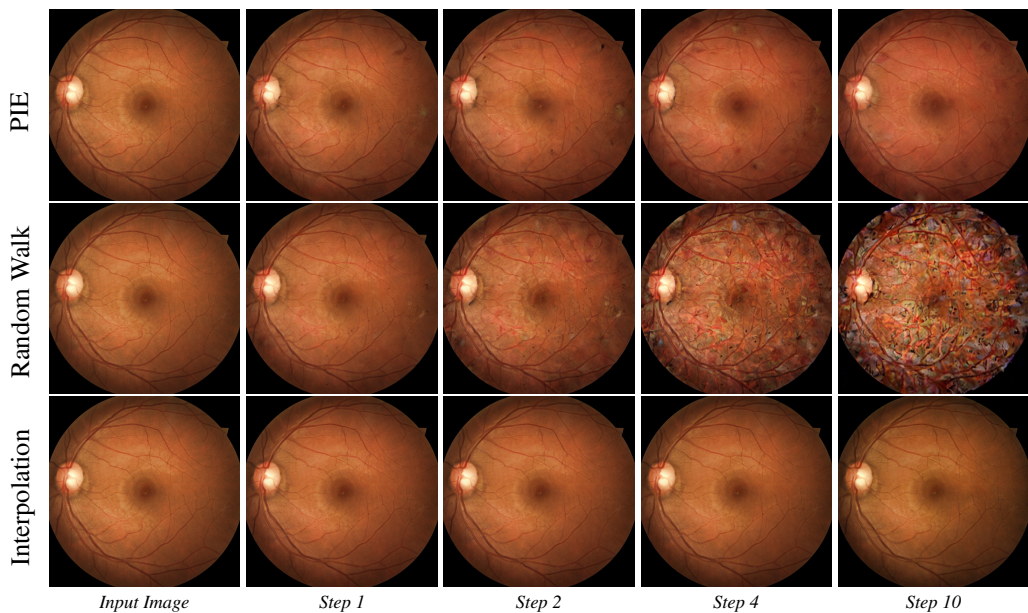


Figure 10: Visualization of PIE, SD Walk, Extrapolation to generate disease progression from Diabetic Retinopathy clinical reports.

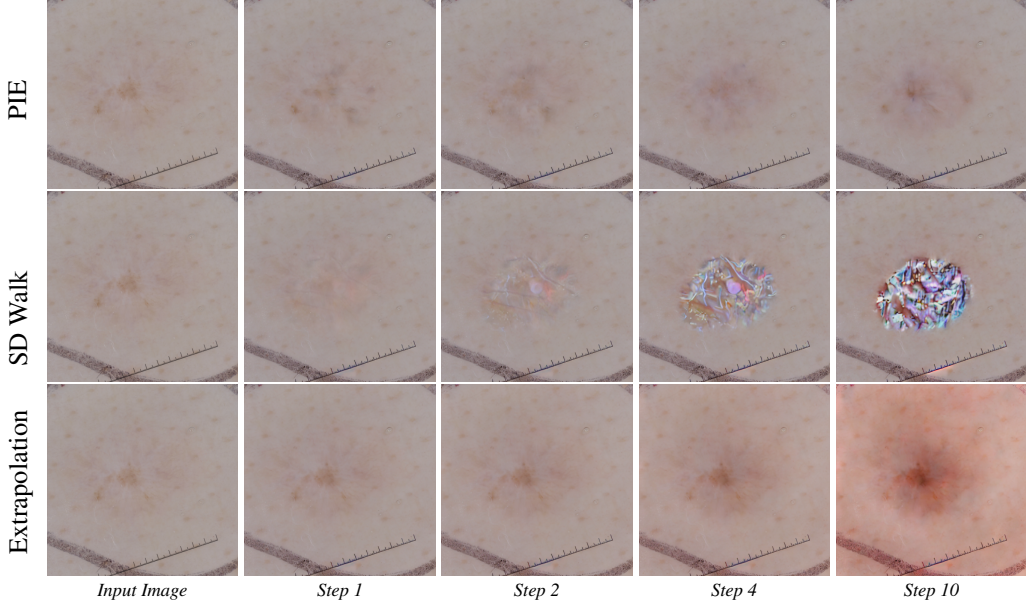


Figure 11: Visualization of PIE, SD Walk, Extrapolation to generate disease progression from Melanocytic Nevi clinical reports.

D.1 Visualization for Three Medical Imaging Domains

To provide an in-depth understanding of how PIE performs during different disease progression inference scenarios compared to baseline models, we present detailed visualizations demonstrating PIE’s advantages. PIE consistently maintains the realism of the input image even after 10 steps of progression, excelling in most scenarios. Figure 9 displays a comparison among three methods simulating Cardiomégalie progression. PIE outperforms both SD Walk and Extrapolation by expanding the heart without introducing noise after 2 steps. Figure 10 displays a comparison among three methods simulating Diabetic Retinopathy progression. PIE outperforms both SD Walk and Extrapolation by adding more bleeding (red) and small blind (white) regions without introducing noise after 2 steps. Figure 11 displays a comparison among three methods simulating Melanocytic Nevi progression. PIE outperforms the other two methods as it keeps the color and shape of the patient’s skin but continually enhance the feature for Melanocytic Nevi.

SD Walk, while it can interpolate within the prompt latent space, tends to generate noise. Although it can generate convincing video sequences in the general domain, it struggles to simulate authentic disease progression. On the other hand, Extrapolation, despite being effective for bone X-rays, faces challenges with more complex medical imaging domains like chest X-rays. Extrapolation’s editing process is considerably slower than the other two methods, and it fails to be controlled effectively by clinical reports.

Co-occurring diseases. PIE is capable of generating images for co-occurring diseases, although the performance slightly trails behind that of single disease generation. Figure 12 illustrates an example of disease progression simulation for co-occurring Cardiomégalie, Edema, and Pleural Effusion. The progression for Cardiomégalie and Pleural Effusion escalates rapidly at the initial stages, whereas Edema develops more slowly. However, after 10 steps, Edema achieves a high confidence score, indicating successful simulation despite its slower growth.

D.2 Failure Case Analysis

Despite outperforming baseline models, PIE still faces limitations tied to data sensitivity issues. For instance, imbalances in the distribution of training data for Stable Diffusion can limit PIE’s capability to edit rare diseases. In some cases, PIE might generate essential medical device features but fail to preserve them in subsequent stages of progression simulation, as observed with features

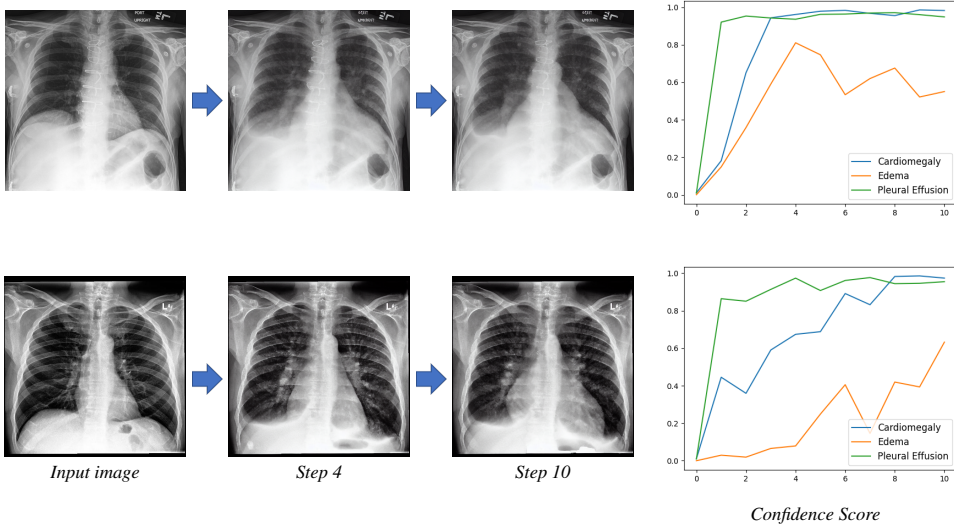


Figure 12: PIE can successfully simulate co-occurring diseases progression (Patient's clinical report shows high probability to be Cardiomegaly, Edema, Pleural Effusion at the same time).



Figure 13: A failure case of the PIE model in preserving the features of a pacemaker during the simulation of Cardiomegaly disease progression. Pacemaker is usually used by patient with severe Cardiomegaly. At Step n-1, the X-ray displays an electronic line. At Step n, both the electronic line and the pacemaker are visible. However, by Step n+1, all the medical device features, including the pacemaker, have vanished from the simulation. It's important to note that the input clinical prompt did not contain any information regarding the pacemaker, making it difficult for the model to retain this crucial feature. This illustrates the challenges faced by models like PIE in dealing with significant but unmentioned clinical features in the input data. It underscores the need for incorporating comprehensive and detailed clinical data to ensure accurate and realistic disease progression simulations.

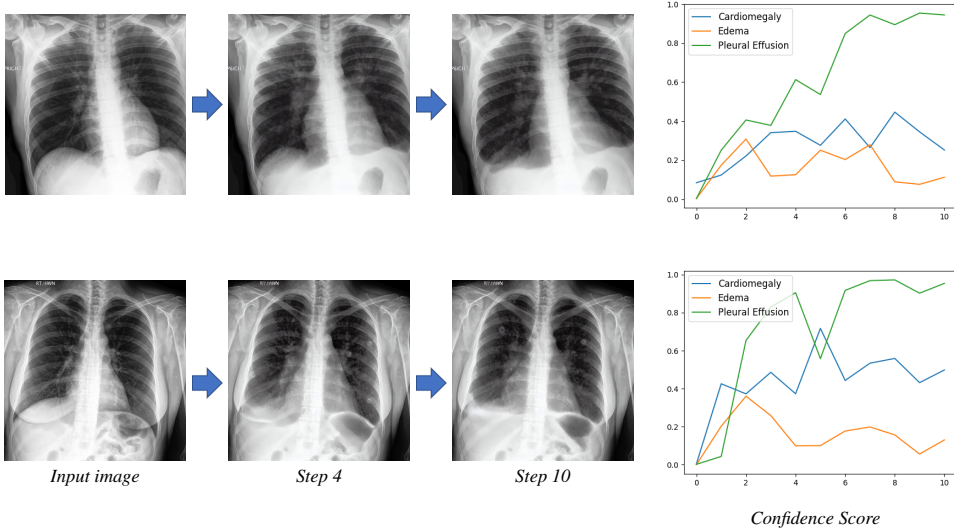


Figure 14: Two failure cases of the PIE model in simulating co-occurring diseases progression for Cardiomegaly, Edema, and Pleural Effusion, only the features for Pleural Effusion are captured. These failure cases arise from the issue related to imbalanced label distribution in the training data. Specifically, the prevalence of Pleural Effusion is significantly higher than the other four classes, leading to an inherent bias in the model’s simulations for co-occurring diseases. This imbalance emphasizes the need for a more diversified and balanced training dataset for more accurate simulation of co-occurring diseases.

like pacemakers. Figure 13 shows a good example of pacemaker disappearance during simulation. Besides, the co-occurring diseases simulation also has some failure cases (see Figure 14).

Fundamentally, these shortcomings could be addressed with a larger and label-equal distribution dataset. However, given that the volume of medical data is often smaller than in other domains, it is also important to explore fine-tuning PIE’s diffusion backbone through few-shot learning under extremely imbalanced label distribution.

D.3 Hyperparameter Search & Analysis

While the Fréchet Inception Distance (FID) and Kernel Inception Distance (KID) metrics are widely utilized in the evaluation of generative models, they do not necessarily align with the perceptual quality of images, making them unsuitable for evaluating progression simulation tasks. Nevertheless, for the subsequent hyperparameter search and ablation study, we added the results of KID score, given its ability to provide insight into the diversity and distributional closeness of the generated images in relation to the real data.

To demonstrate the significance of the ROI mask as a key control factor in the PIE, an experiment was conducted to compare the performance of models using and not using ROI masks across three domains, with each model tested using 5 different random seeds. The evaluation focused on the classification confidence score and CLIP score. Results, as shown in Table 3, revealed that while removing the ROI mask could sometimes increase the confidence score (observed for chest X-ray and skin imaging), it consistently led to a decrease in the CLIP score. Further visual analysis depicted in Figure 15 shows that the ROI mask crucially helps in preserving the basic shape of the medical imaging during the PIE process. Consequently, these findings suggest that the ROI mask, alongside clinical reports, serves as a critical medical prior for simulating disease progression. It helps the PIE to concentrate on disease-related regions while maintaining the realism of the input image.

We present a comprehensive examination of various hyperparameters, namely strength (γ in Algorithm 1), step (N), β_1 , and β_2 , and their respective tradeoffs as demonstrated in tables 4, 5, and 6. Notably, a discernible tradeoff exists between classification confidence score and CLIP-I/KID,

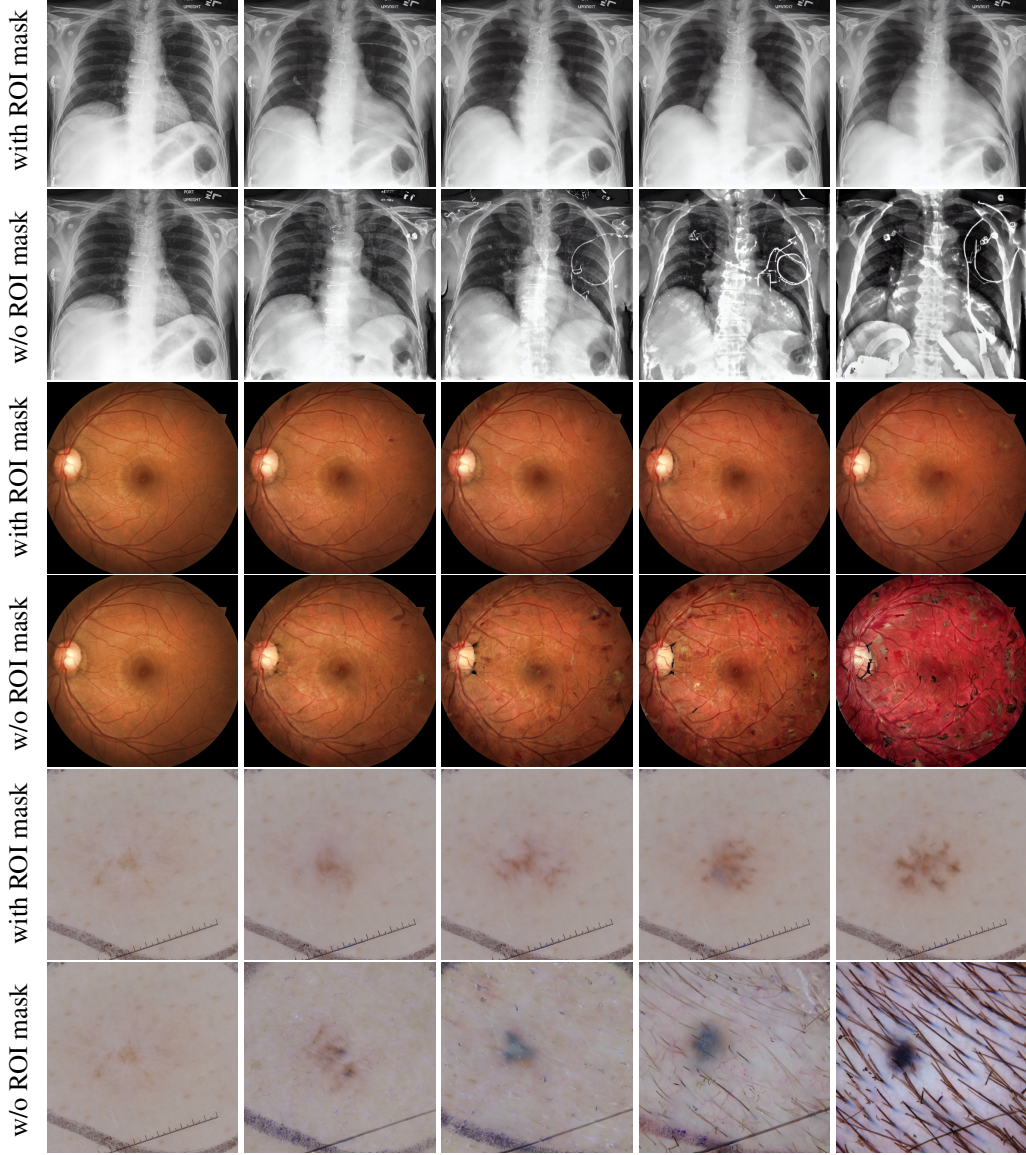


Figure 15: Visualization comparison between ROI mask influence for three medical imaging domains.

wherein an increase in classification confidence score results in a decrease in CLIP-I. In the subsequent section, we offer an intricate analysis of each hyperparameter.

Table 4 illustrates a positive correlation between the strength of PIE and classification confidence score, while revealing a negative relationship between strength and CLIP-I/KID. From an intuitive standpoint, as the strength of PIE increases, more features are directed to align with the pathologies within the original images. Consequently, the classifier exhibits greater confidence in accurately predicting the specific disease class, leading to a more significant deviation from the initial starting point. As a result, the classification confidence score value increases while the CLIP-I value decreases, reflecting the inverse relationship between the two metrics.

Table 5 presents a similar pattern initially. However, both classification confidence score and CLIP-I/KID reach a state of stability after a certain number of steps. This observation aligns with our theoretical analysis as outlined in Proposition 2. Moreover, it can be interpreted as the convergence of a Cauchy geometric sequence, wherein the discrepancy between successive steps gradually diminishes as the value of N tends towards infinity.

Lastly, in Table 6, we explore the interplay between β_1 and β_2 , which serve as parameters governing the rate of progression within and outside the region of interest (ROI) respectively. Our findings reveal that β_2 , responsible for regulating the pace of progression within the ROI, exerts a more pronounced influence on classification confidence score, while β_1 exhibits a stronger impact on CLIP-I/KID. This outcome can be intuitively comprehended, considering that the ROI typically encompasses a smaller area of paramount importance for aligning with disease-specific features. Conversely, the areas outside the ROI exert a significantly greater influence on the realism captured by CLIP-I/KID.

In summary, our study elucidates the inherent trade-offs and offers valuable practical insights, thereby furnishing meaningful guidance for effectively utilizing PIE in practice.

Table 3: Mask, w/o mask guidance comparisons.

Method	Chest X-ray		Retinopathy		Skin Lesion Image	
	Conf (↑)	CLIP-I (↑)	Conf (↑)	CLIP-I (↑)	Conf (↑)	CLIP-I (↑)
w/o mask	0.729	0.93	0.163	0.96	0.666	0.85
with mask	0.690	0.96	0.807	0.99	0.453	0.95

Table 4: Strength γ selection for $N = 10$.

Strength	Conf (↑)	CLIP-I (↑)	KID (↓)
0.05	0.038	0.966	0.0685
0.1	0.120	0.969	0.0638
0.2	0.273	0.969	0.0885
0.3	0.455	0.967	0.1033
0.4	0.746	0.965	0.1142
0.5	0.977	0.962	0.1389
0.6	0.995	0.956	0.1549
0.7	0.998	0.955	0.1533
0.8	0.999	0.951	0.1629

Table 5: Simulation steps N selection with $\gamma = 0.5$.

Step (N)	Conf (↑)	CLIP-I (↑)	KID (↓)
1	0.491	0.965	0.094
2	0.731	0.964	0.098
5	0.881	0.963	0.121
10	0.978	0.962	0.142
20	0.989	0.961	0.111
50	0.975	0.962	0.130
100	0.959	0.962	0.115

E User Study

E.1 Questionnair

The questionnaire includes 2 parts. Part one consists of 20 multiple choices of single image classifications, 10 single-step generations, and 10 real X-ray images sampled from the training set. Part two consists of 3 generated disease progressions consisting of Cardiomegaly, Edema as well Pleural Effusion. Each progression runs 10 steps. For each single image classification, we ask "Please determine the pathologies of the following patient" and let the user pick from 6 options {No findings, Cardiomegaly, Consolidation, Edema, Effusion, Atelectasis} with possible co-occurrence, while for each of the 10-step progressions, we ask "Does the below disease progression fit your expectation?" and let the user input a binary answer of yes or no.

Table 6: Beta selection.

β_1	β_2	Conf (\uparrow)	CLIP-I (\uparrow)	KID (\downarrow)
0.01	1.0	0.954	0.946	0.133
0.01	0.75	0.977	0.948	0.140
0.01	0.5	0.554	0.965	0.090
0.1	1.0	0.960	0.965	0.126
0.1	0.75	0.976	0.962	0.140
0.1	0.5	0.554	0.962	0.089
0.2	1.0	0.963	0.947	0.134
0.2	0.75	0.977	0.964	0.137
0.2	0.5	0.556	0.962	0.089

Below we include the full instructions we gave for our user study both in English and Chinese. Here we only include the English version.

1. Please read the instruction and inspect the images carefully before answering.
2. Please provide your years of experience
3. For the first 20 questions, please determine the pathologies from the X-ray images (you can choose more than one answer). For the last 3 questions, please answer if the disease progression shown fits your expectation.

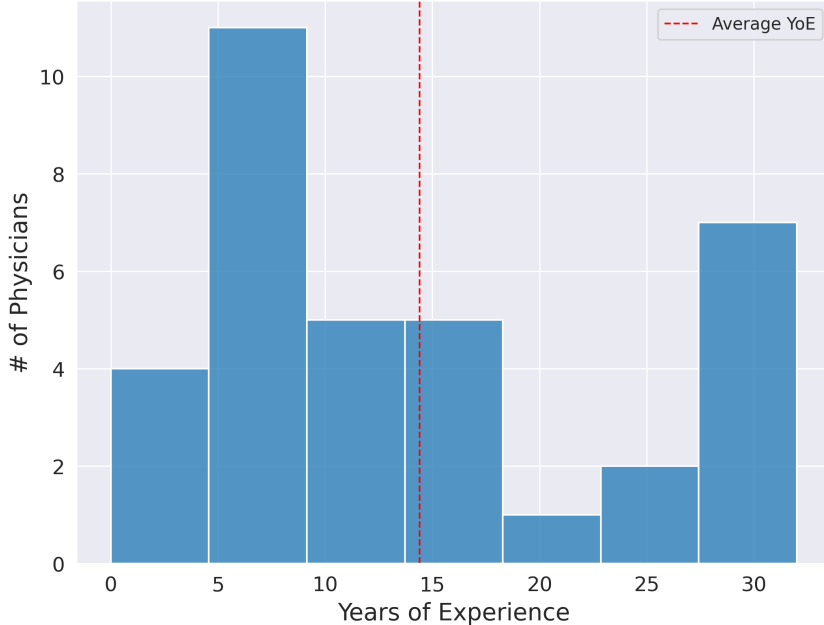


Figure 16: The distribution of the years of experience from the group of physicians who participated in the user study. The average number of years of experience is 14.4 years. Over half of the group have more than 10 years of experience. This data attest that our surveyees are highly professional and experienced.

E.2 Statistics

To show the significance of our findings, we perform the paired t-test on the F1 scores of real and generated scans over the 35 users. Our finding is significant with a p-value of 0.0038.

24 请判断下图的病症
(Please determine the pathologies of following patient)
可以多选 (Multiple choice)

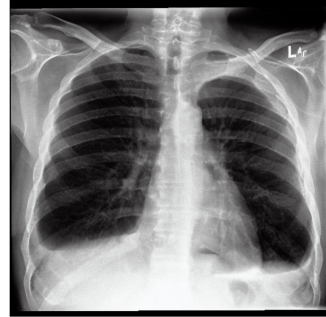


Choose as many as you like

- A 健康 (No findings)
- B 心脏肥大 (Cardiomegaly)
- C 肺实变 (Consolidation)
- D 肺水肿 (Edema)
- E 胸腔积液 (Effusion)
- F 肺塌陷 (Atelectasis)

[Add choice](#)

24 以下病例的进程是否符合临床预期?
(Does the below disease progression fit your expectation?)
从轻微到严重
(From mild to severe)



A 符合 (Yes)

B 不符合 (No)

[Add choice](#)

Figure 17: Example of User Study I: we ask the physicians to pick from the 6 options and it's possible to pick more than one option.

Figure 18: Example of User Study II: we ask the physicians to decide if the generated progression of the disease is credible or not.

To quantitatively analyze their responses, we treat each class of pathologies as an independent class and compute precision, recall, and F1 over all the pathologies and physicians.

F Discussion

F.1 Limitations and Societal Impacts

The proposed framework is subject to several limitations, with one of the primary constraints being the limited scope of Stable Diffusion. Due to the model's pre-training on general domain data, the absence of detailed medical reports poses a significant challenge to the model's ability to accurately and reliably edit medical images based on precise text conditioning. Moreover, the framework's overall performance may be influenced by the quality and quantity of available data, which can limit the model's accuracy and generalizability. Furthermore, the absence of surgical or drug intervention data further restricts the framework's ability to simulate medical interventions. Moving forward, it would be beneficial to explore ways of integrating more detailed descriptions of medical data in the fine-tuning process of Stable Diffusion to improve the framework's performance and precision in disease simulation through text conditioning. Additional details on the framework's limitations, including an analysis of failure cases, can be found in Supplementary D.

Progressive Image Editing (PIE) holds promise as a technology for simulating disease progression, but it also raises concerns regarding potential negative social impacts. One crucial concern revolves around the ethical use of medical imaging data, which may give rise to privacy and security issues. To address this, healthcare providers must take measures to safeguard patient privacy and data security when utilizing PIE. An effective mitigation strategy involves employing anonymized or de-identified medical imaging data, while also adhering to ethical guidelines and regulations like those outlined by HIPAA (Health Insurance Portability and Accountability Act).

Another concern relates to the accuracy of the simulations generated by the framework, as errors could lead to misdiagnosis or incorrect treatment decisions. To alleviate this concern, rigorous testing and evaluation of the technology must be conducted before its implementation in a clinical setting. Enhancing the accuracy of simulations can be achieved by incorporating additional data sources, such as patient history, clinical notes, and laboratory test results. Additionally, healthcare providers should receive adequate training on effectively utilizing the technology and interpreting its results.

Discrimination against certain groups, based on factors such as race, gender, or age, poses yet another potential concern. Healthcare providers must ensure the fair and unbiased use of the technology. This can be accomplished by integrating diversity and inclusion considerations into the technology's development and training processes, as well as regular monitoring and auditing its usage to identify any signs of bias or discrimination.

The cost and accessibility of the technology present further concerns, potentially restricting its availability to specific groups or geographic regions. To tackle this issue, healthcare providers should strive to make the technology accessible and affordable to all patients, regardless of socioeconomic status or geographic location. This can be achieved through the creation of cost-effective models, partnerships with healthcare providers, and government funding initiatives.

Lastly, there is a risk of excessive reliance on technology, leading to a diminished reliance on clinical judgment and expertise. To mitigate this concern, healthcare providers must be trained to view the technology as a tool that complements their clinical judgment and expertise, rather than relying solely on it for diagnostic or treatment decisions. The technology should be used in conjunction with other data sources and clinical expertise to ensure a comprehensive understanding of disease progression.

In conclusion, while the use of PIE comes with potential negative social impacts, there are viable mitigations that can address these concerns. Healthcare providers must be aware of the ethical implications associated with this technology and take appropriate measures to ensure its safe and responsible utilization.